InSAR-derived Coseismic Deformation of the 2010 Southeastern Iran Earthquake (M6.5) and its Relationship with the Tectonic Background in the South of Lut Block

Tomokazu KOBAYASHI, Mikio TOBITA, Akira SUZUKI and Yuko NOGUCHI

Abstract

An inland crustal earthquake with a magnitude of 6.5 that occurred in the southeast of Iran on December 20, 2010 ruptured an unknown fault at depth. Applying interferometric SAR (InSAR) analysis using ALOS/PALSAR data to the earthquake, we detected the coseismic signal from both ascending orbit interferogram of fine beam mode and descending orbit interferogram of ScanSAR mode. Our preferred fault model, assuming a rectangular fault with a uniform slip, shows a nearly pure dextral fault motion with NE-SW-oriented strike. The estimated moment magnitude is 6.6. The fault of the mainshock is on the southern extension of the Kahurak fault, suggesting that the causative fault of this event is probably the identical fault system to the Kahurak fault.

1. Introduction

Iran is subjected to a convergent stress produced by a motion of the Arabian plate in a NNE-SSW direction at a few cm/year relative to the Eurasian plate. The crustal strain caused by the plate convergence is accommodated by inland active faults. In the central and eastern Iran, the plate motion is relatively larger at the west than at the east (see blue arrows in Fig. 1), culminating in a right-lateral shear stress field. Two major fault zones have been developed with a nearly north-south-oriented strike along the western and eastern borders of the Lut Block (Freund 1970; Mohajer-Ashajai et al., 1975; Tirrul et al., 1983; Berberian and Yeats, 1999; Walker and Jackson, 2002), whose fault motions are of right-lateral as they reflect the subjected stress (Walker and Jackson, 2004; Meyer and Le Dortz., 2007).

The earthquake with a magnitude 6.5 (U. S. Geological Survey, 2010) struck the southeast of Iran on December 20, 2010. The epicenter of the main shock was located in the vicinity of the 2003 Bam earthquake. Iran has been historically subjected to large earthquakes due to the active tectonic background. However, in the region where the M6.5 event occurred, no remarkable active fault is identified and the seismicity is relatively less active (Fig. 1). Thus, little is known about the detailed contemporary deformation in the south of Lut Block. For the seismological and tectonics studies of southeastern Iran, it is surely helpful to understand how the seismic event is related to the existing fault system and the surrounding tectonics.

Satellite synthetic aperture radar (SAR) data can provide detailed and spatially comprehensive ground information, and an interferometric SAR (InSAR) enables us to measure ground deformation with high precision (e.g., Massonnet and Feigl, 1998; Bürgmann *et al.*, 2000). We can analyze the detailed source properties by using the high spatial resolution data which provides us with the detailed crustal deformation distribution for moderate-sized earthquakes.

We conducted the InSAR analysis using Advanced Land Observing Satellite (ALOS)/PALSAR data to the M6.5 inland earthquake. The purpose of this paper is to obtain the crustal deformation associated with the earthquake and to construct a fault model on the basis of the InSAR-derived data. We finally discuss the earthquake in relation to the seismotectonics in the south of the Lut Block.

2. SAR Data Analysis

To obtain the coseismic deformation, we used Advanced Land Observation Satellite (ALOS) PALSAR data acquired on September 30, 2010 and December 31, 2010 from ascending path 559 and on July 13, 2010 and January 13, 2011 from descending path 208. The ascending path images in the fine beam (FB) polarization mode were produced to generate a coseismic

interferogram using the conventional range-Doppler algorithm and the two-pass InSAR method (Massonnet and Feigl, 1995; Rosen et al., 2000). For the descending orbit, FB observation, which is a normal operational mode of ALOS/PALSAR, was not conducted for the source region after the earthquake, thus we compensated

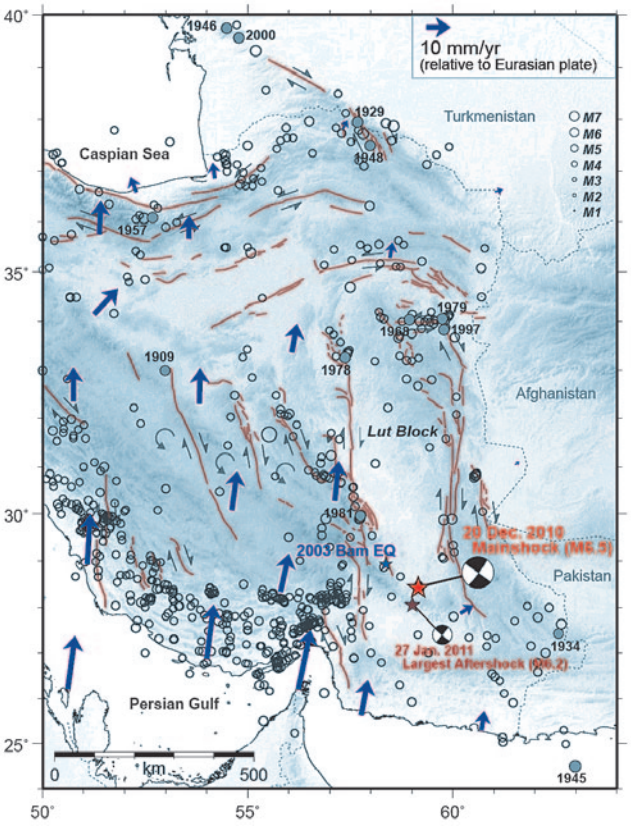

Fig.1 The seismicity map and tectonic setting of central and eastern Iran. Large and small red stars stand for the epicenters of earthquake on December 20, 2010 (M6.5) and the largest aftershock (M6.2) on January 27, 2011, respectively. Active fault traces (Walker and Jackson, 2004) are indicated by brown lines with arrows showing their fault motions. Blue arrows represent GPS-derived velocities relative to the Eurasian plate (Vernant et al., 2004). Open and closed circles indicate earthquakes of M>5 and remarkable large historical earthquakes (M>7) since 1900, respectively. Beach balls represent the centroid-moment-tensor (CMT) solution.

for the lack of descending orbit observation data by using ScanSAR data. For the preprocessing, we used a self-developed program, which extracts five beam data files from a ScanSAR raw data file and pads zeros between bursts; thereafter, the program resamples the data in order to even the azimuth time interval between the master and the slave images. This ScanSAR preprocessing program has been applied successfully to several seismic events such as the 2010 Yushu earthquake (Tobita et al, 2011). Two optical sensors onboard ALOS are essentially operated in descending orbit, thus PALSAR data acquisition in descending orbit is rare. Wide coverage of PALSAR ScanSAR data is effective in increasing the frequency of InSAR observations of specific locations on the earth and providing increased opportunities for acquiring both ascending and descending path data. Observations conducted from two opposite directions with ascending and descending orbits can provide us with two orthogonal displacement components that are composed of quasi-vertical and horizontal movements; a 2.5D analysis (described later), enables us to infer the type of fault motion easily.

We processed the ALOS/PALSAR data using GSISAR software (Fujiwara and Tobita, 1999; Tobita *et al.*, 1999; Fujiwara *et al.*, 1999; Tobita, 2003). The topographic phase was removed by the two-pass InSAR method using the 90-m-spacing Shuttle Radar Topography Mission (SRTM) DEM. The perpendicular baselines that affect interferogram coherence were +179 m and +1080 m for the ascending and descending interferograms, respectively. Obvious long-wavelength residual phases, which are probably attributed to ionospheric disturbance, were seen in the interferograms. We assumed that far-field displacement was zero and that the residual phases were expressed by a biquadratic surface. Thus, we were able to successfully flatten the descending interferogram without removing significant displacement signals.

3. Coseismic displacement map by InSAR

Figure 2 shows unwrapped interferograms. The coherence is high for the most part. This is probably due to the result of the less-vegetated arid environment and the consequently low surface displacement gradient. An intensive deformation is located approximately 100 km southeast from the epicenter of the 2003 Bam earthquake. Two clear fringes with a pair of slant range lengthening and shortening are observed in the results of both ascending and descending data. For the ascending data, the movements of the western and the eastern fringes

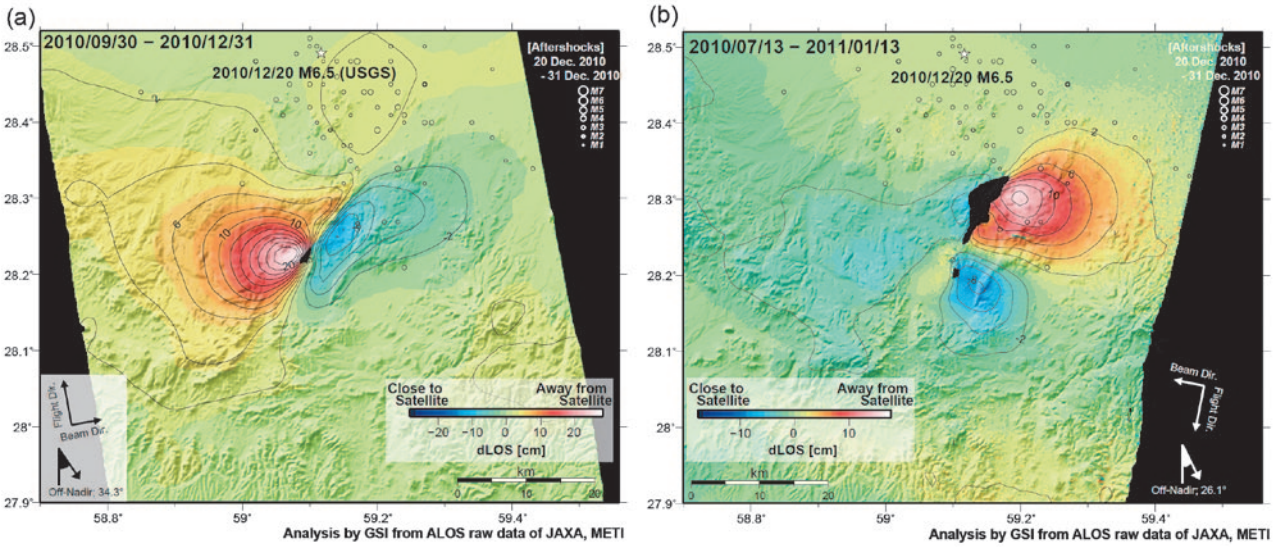

Fig.2 Unwrapped interferograms for the earthquake on December 20, 2010 (M6.5). (a) Ascending interferogram of strip-map mode. (b) Descending interferogram of ScanSAR mode. A star indicates the USGS-NEIC's epicenter (U. S. Geological Survey, 2010).

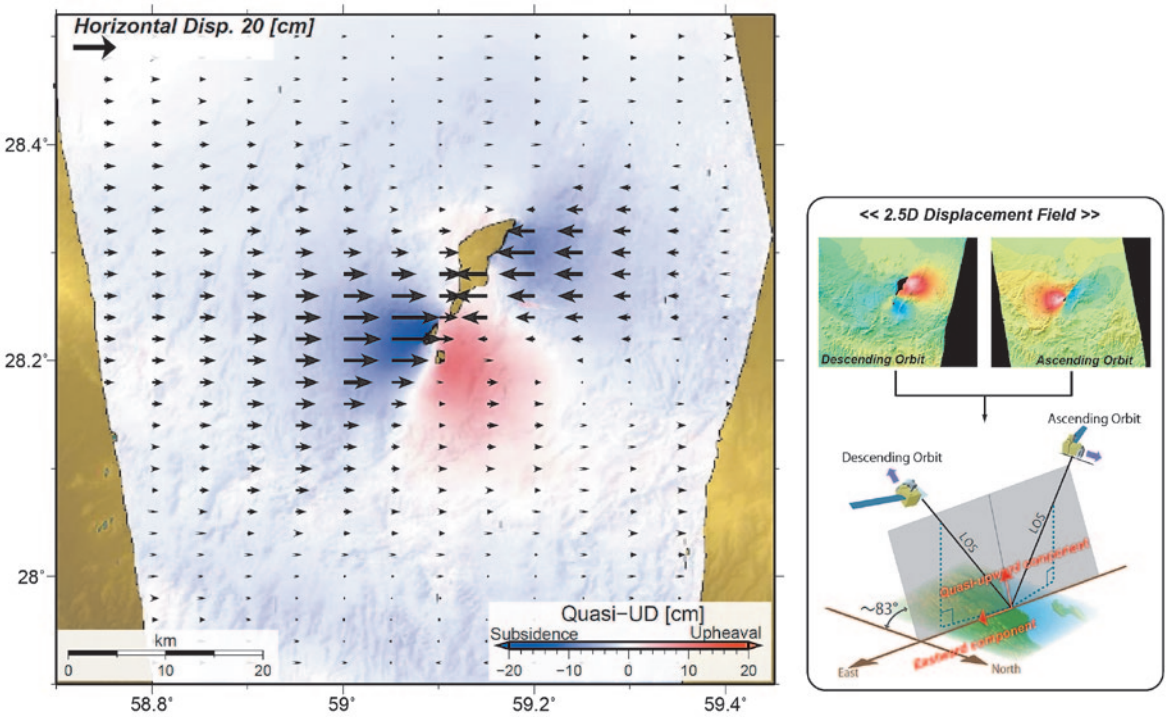

Fig.3 The 2.5D displacement field. Arrows indicate EW component of coseismic displacement. Warm and cold colors represent uplift and subsidence, respectively. Inset of right bottom shows a schematic diagram for 2.5D displacement analysis.

in the deformation area are away from the satellite with approximately 25 cm and close to the satellite with approximately 11 cm at maximum, respectively. The movements of the northern and the southern fringes for the descending data are away from the satellite with approximately 15 cm and close to the satellite with approximately 8 cm at maximum, respectively. The deformation area distributes ~20 km away from the epicenter determined by seismic data (a white star), suggesting that the actual epicenter is evidently located further south.

By combining the ascending and descending data, we conducted the 2.5D analysis (Fujiwara et al., 2000) to obtain EW and quasi-vertical component (elevation

angle of 2.5D plane = ~83°) (see Fig. 3). Eastward and westward motions are evaluated to be ~26 cm and ~21 cm at maximum, respectively. The vertical displacement field shows a quadrant-like distribution pattern, although the displacement in the northwest cannot be identified clearly due to incoherence. Upheaval is observed in the southeast with ~11 cm at maximum, while subsidence is observed in both the southwest and the northeast with ~17 cm at maximum. Convergence line of horizontal displacement across which the ground movement is in the opposite direction extends in the northeast-southwest orientation, which makes us infer that the orientation of fault strike is the northeast-southwest rather than the northwest-southeast. Note that, with no elaborated modeling work, we are able to estimate the nodal plane from the simple analysis using InSAR data, which cannot be determined from the seismic data such as beach balls (Fig.1) and aftershock distribution (Fig. 2).

4. Fault model

On the basis of the interferogram data, we constructed a fault model under an assumption of a rectangular fault with a uniform slip in an elastic half-space (Okada, 1992). The interferograms have ground surface changes on several dozen km range, producing too many values to be easily assimilated in a modeling scheme. In order to reduce the number of data for the modelling analysis, we resampled the interferogram data in advance, using a quadtree decomposition method. Essentially, we followed an algorithm presented by Jónsson et al. (2002). For a given quadrant, if, after removing the mean, the residue is greater than a prescribed threshold (1 cm in our case), the quadrant is further divided into four new quadrants. This process is iterated until either each block meets the specified criterion, or until the quadrant reaches a minimum block size (8 × 8 pixels for these data). Upon application of the above-mentioned procedure, the sizes of the respective interferogram data sets were reduced from ~1.3 million to 316 for path 559 and from ~4.6 million to 1674 for path 209.

We applied a simulated annealing method for searching optimal fault parameters (e.g., Cervelli *et al.*, 2001). We randomly used parameters within a search range of 59.05° to 59.20° in longitude, 28.15° to 28.30° in latitude, 0.1 to 15 km in depth, 1 to 30 km in length, 1 to 15 km in width, 20° to 60° (200° to 240°) in strike, 50° to 90° in dip, -180° to 180° in rake, and 0 to 5 m in slip. At present, with a priori knowledge of the orientation of fault strike estimated from 2.5D displacement field, we assumed a fault plane with a strike of northeast-southwest. To estimate the individual confidence of inferred parameters, we employed a bootstrap method (Efron, 1979).

Figure 4 shows the line-of-sight (LOS) displacement calculated using our preferred model and the residuals between the observations and the calculations. Regardless of a simple fault model with a uniform slip on a planar fault, our fault model is able to reconcile the observations well for both the ascending (Figs. 4: (a) and (b)) and the descending data (Figs. 4: (c) and (d)). We stress that the derived fault model sufficiently picks up the nature of the source property without aimlessly increasing number of free parameters by more elaborate modeling such as a slip distribution model. Estimated fault parameters and their errors are listed in Table 1. The moment is estimated to be 9.07×10^{18} Nm, equivalent to M_w6.6 with a rigidity of 40 GPa, consistent with that determined by seismic data (Global CMT projection: 8.38×10^{18} Nm (M_w6.5); USGS CMT: 1.2×10^{19} Nm (M_w6.7)). Our fault model shows (1) a nearly vertical fault plane (dip angle: 89.4°), (2) a NE-SW strike direction (strike angle: N29.0°E), and (3) a nearly pure right-lateral fault motion (rake angle: 175.4°). The right-lateral slip is consistent with the regional tectonics (Fig. 1).

Figure 5 shows the variation of solutions derived through the bootstrap approach, that is, the accuracy of determination of fault parameters. The standard deviations are listed in parentheses of Table 1. The dip, the strike, and the rake are constrained well with the 2 σ errors of ~7°, ~10°, and ~16°, respectively. Thus we are able to determine that the above-mentioned features on the model are reliable. The estimated fault depth ranges 3.4 to 6.4 km with a 2 σ error (~95 % confidence), therefore there is a significant difference from that

determined seismic data (USGS: 11 km). If the source depth was 11.8 km (USGS), it yielded only ~8 cm in ΔLOS displacement at maximum when assuming a slip equivalent to M_w6.6. It demonstrates that the InSAR observation contributes to obtain exact source depth of rupture. The obtained InSAR and the InSAR-based fault model data provide the detailed seismic source property regarding the rupture location, the orientation of fault plane, and the direction of slip with high accuracy. On the other hand, the size of fault (length and width) and the amount of slip are not necessarily determined well with a trade-off among them (Fig. 5).

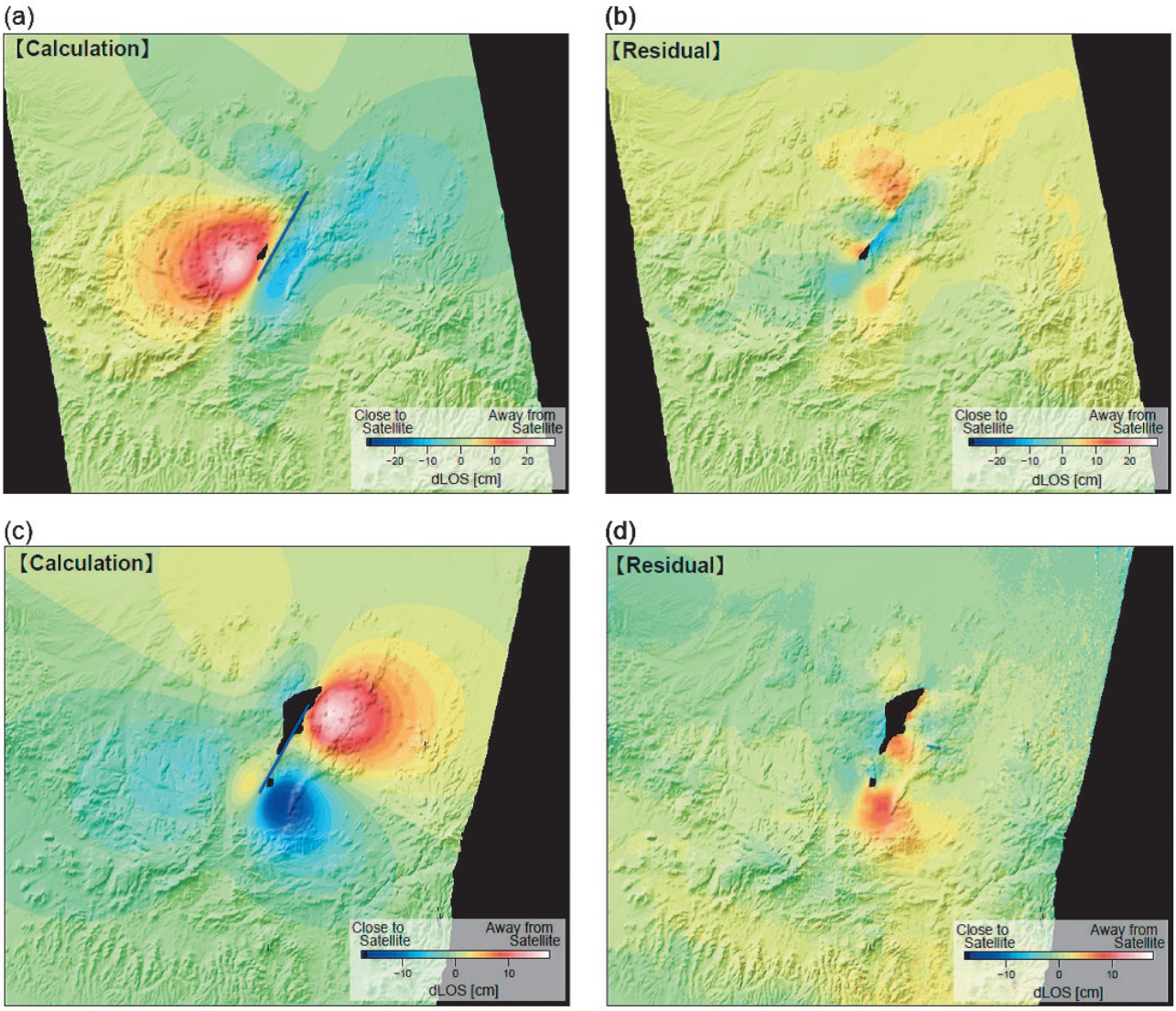

Fig.4 The LOS displacement change calculated from the inferred fault model for ascending data (a) and for the descending data (c). The residuals between observations and calculations for the ascending data (b) and for the descending data (d). Solid lines on calculated interferograms represent the inferred fault projected on the ground.

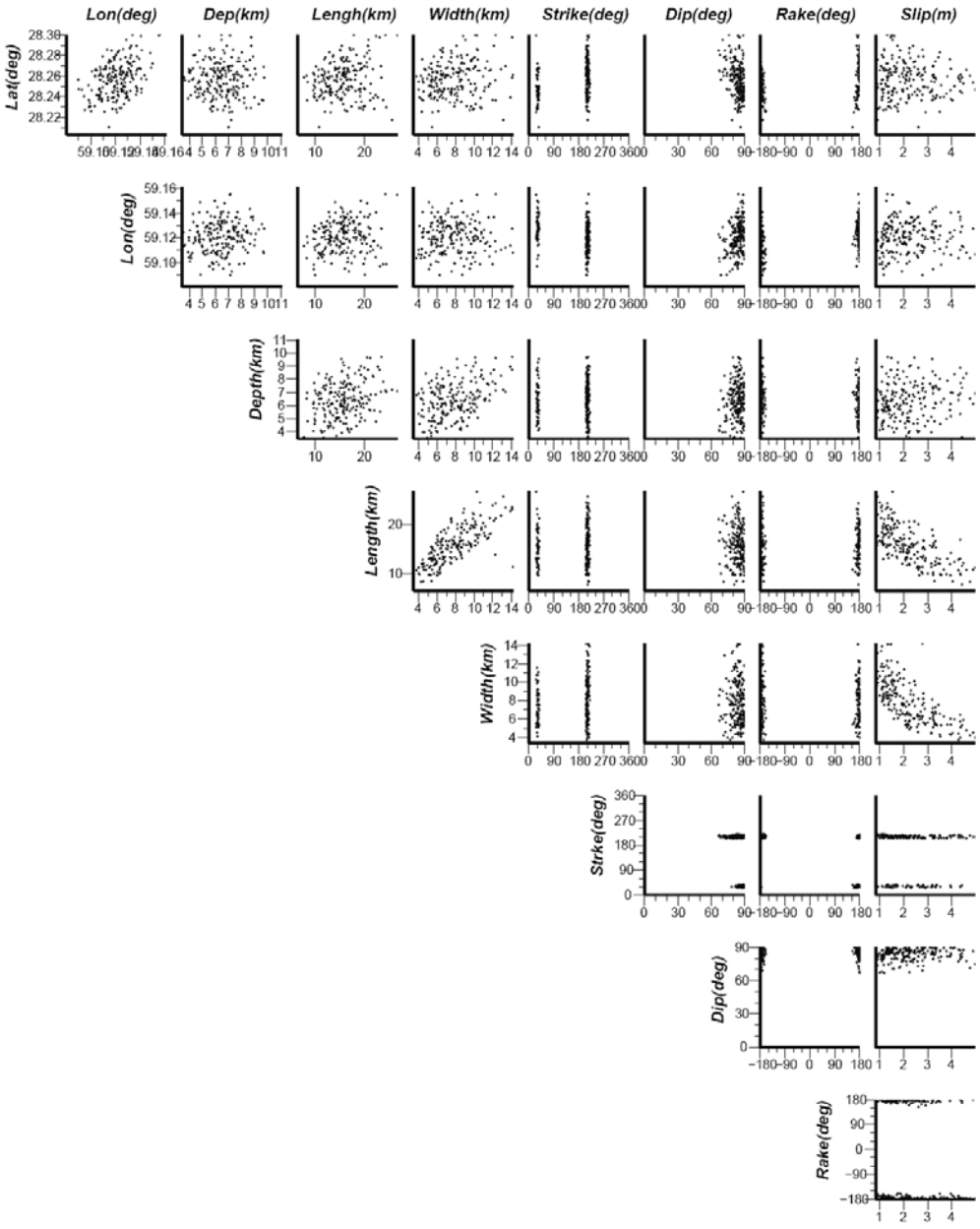

Fig.5 Variation of fault parameter estimates obtained from a bootstrap approach.

Table 1 Preferred fault model parameters for the mainshock on December 20, 2010. We define the location of each fault as its center. The units are: meter for length, width and depth, degrees for dip, strike and rake, and meters for slip. The values in parenthesis are standard deviations for the individual fault parameters calculated by a bootstrap approach.

Longitude	Latitude	Depth	Length	Width	Strike	Dip	Rake	Slip
59.125	28.248	5.0	14.9	5.2	29.0	89.4	175.4	2.9
(0.013)	(0.017)	(1.4)	(3.8)	(5.2)	(3.4)	(5.2)	(8.1)	(1.0)

5. Crustal deformation after the mainshock

We further conducted InSAR analyses for the data acquired after the mainshock. Figure 6 shows the obtained unwrapped interferogram for the 46 days from December 31, 2010 to February 15, 2011. We can recognize clear ground displacements with ~10 cm peak-to-peak in LOS direction. The intensive crustal deformation area is obviously distant southwestwardly from the coseismic deformation area, suggesting that the causative fault slips are spatially isolated between the

two areas. The observed ground surface displacement is probably produced by the largest aftershock (M6.2) on January 27, 2011.We further analyzed other SAR data pair acquired on February 15, 2011 and April 2, 2011, however, no significant surface displacement exceeding the signal-to-noise ratio is observed (Fig. 7).

We model the fault slip by producing the ground displacement as shown in Fig. 6, in the same manner as coseismic fault modeling. According to the result of seismic data analysis, the p-axis of the largest aftershock is oriented in an EW direction similar to the mainshock, suggesting a strike-slip fault type. For the seismic event,

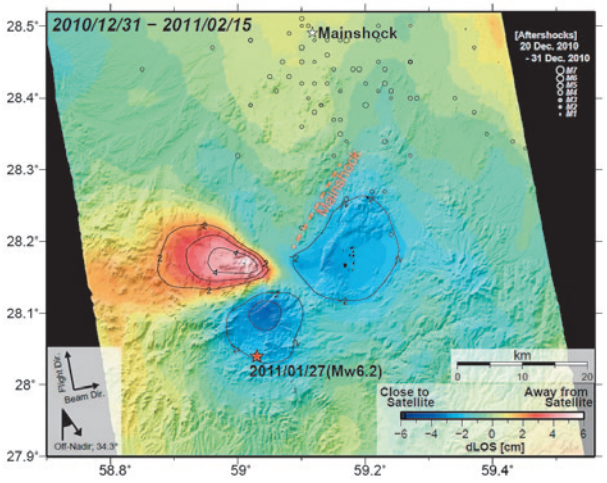

Fig.6 Observed crustal deformation associated with the large aftershock (M6.2) on January 27, 2011. A SAR data pair of December 31, 2010 and February 15, 2011 is used for the analysis. Red star stands for an epicenter of the largest aftershock. Open circles indicate aftershocks from December 20 to December 31, 2010. Red broken line represents the inferred fault projected on the ground for the mainshock. Spatial range depicted is same as Fig. 2.

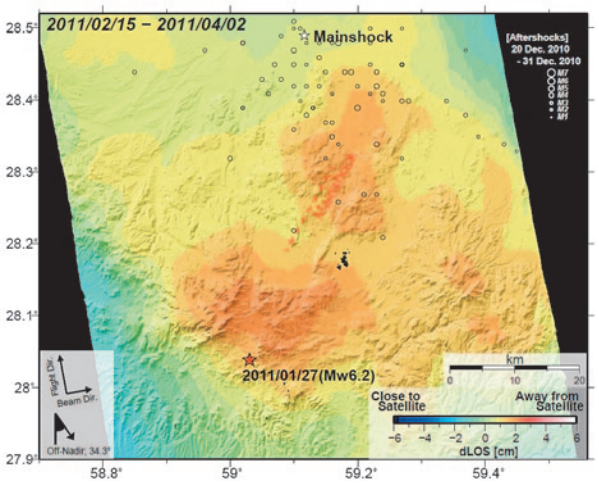

Fig. 7 Interferograms obtained from a SAR data pair of February 15, 2011 and April 2, 2011.

however, there is no descending orbit pair of ALOS/PALSAR. Thus we can hardly infer the nodal plane in advance from the 2.5D analysis. For the modeling analysis, we assumed two types of fault models; a NE-SW striking fault and a NW-SE striking fault. We randomly used parameters within a search range of 20° to 90° (200° to 270°) in strike for the NE-SW fault, and 100° to 170° (280° to 350°) for the NW-SE fault.

Table 2 lists estimated fault parameters and their errors. Figure 8 shows the modeling results for the NE-SW and the NW-SE striking fault. The best solution for the model of NE-SW nodal plane shows a right-lateral slip on a vertical fault plane with the strike of 228°, on the other hand, for the NW-SE nodal plane model a left-lateral slip on a nearly vertical fault plane with the strike of 328° is estimated as the best solution. Theses

Table 2 Preferred fault model parameters for the aftershock (M6.2) of January 27, 2011 for the NE-SW nodal plane (upper) and the NW-SE plane (bottom).

NE-SW nodal plane model								
Longitude	Latitude	Depth	Length	Width	Strike	Dip	Rake	Slip
59.052 (0.013)	28.164 (0.013)	5.7 (1.3)	9.8 (3.4)	4.6 (4.6)	227.9 (5.8)	88.1 (4.1)	176.9 (9.0)	1.4 (1.2)
NW-SE nodal plane model								
Longitude	Latitude	Depth	Length	Width	Strike	Dip	Rake	Slip
59.071 (0.016)	28.161 (0.012)	6.0 (1.4)	7.9 (3.3)	4.8 (2.1)	328.4 (6.2)	88.4 (6.1)	1.9 (6.3)	1.8 (1.1)

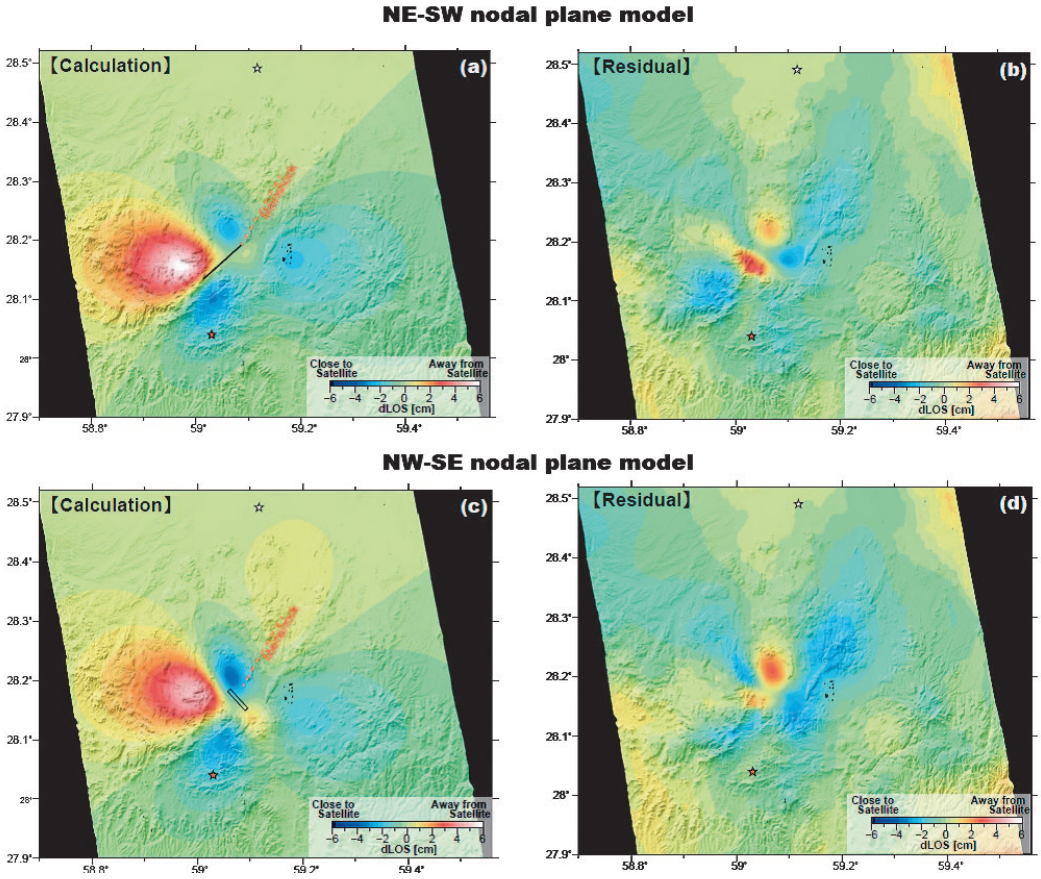

Fig. 8 The LOS displacement changes calculated from the inferred fault models for the largest aftershock ((a) and (c)). The residuals between the observations and the calculations ((b) and (d)). The solid lines represent the inferred fault planes projected on the ground, constructed under assumptions of (a) NE-SW-oriented nodal plane and (c) NW-SE-oriented nodal plane, respectively.

solutions are conjugate. The both models are able to account for the observation well within the residual of ~1 cm although the amount of a few cm at maximum is still remained partly. There is no significant difference between the two models. The analysis result shows that, for this seismic event, we cannot determine the nodal plane uniquely from only the ascending data. Although there remains an ambiguity between the fault plane and the auxiliary plane, we can determine that, similar to the mainshock, this event occurred under the stress condition having a p-axis of an EW orientation. The moment is estimated to be 2.52×10^{18} Nm, equivalent to M_w6.2 for the NE-SW nodal plane model, and to be 2.68×10^{18} Nm, equivalent to M_w6.2 for the NW-SE nodal plane model, with a rigidity of 40 GPa. This value agrees well with the moment derived from seismic data: 2.43×10^{19} Nm (M_w6.2) (Global CMT projection).

6. Relationship with the background strain rate field and the surrounding fault system

To test the relationship with the regional strain field and the fault systems in the southeastern Iran, we roughly estimated the strain rate using GPS data presented by Vernant et al. (2004) (Fig. 1). We now calculate the strain by applying a kriging method (e.g., Kobayashi, 2009). Figure 9 shows the estimated maximum shear strain. The solid lines represent the direction and magnitude of the right-lateral component. Gray lines and arrows are active fault traces and their fault motions, respectively. The orientation of the right-lateral component is in harmony with the existing active fault. The two major fault zones along the eastern and western margins of the Lut Block are just in the relatively strong maximum shear strain field with NS-oriented right-lateral motion. The good spatial relationship suggests that the in situ strain field is favorable for the

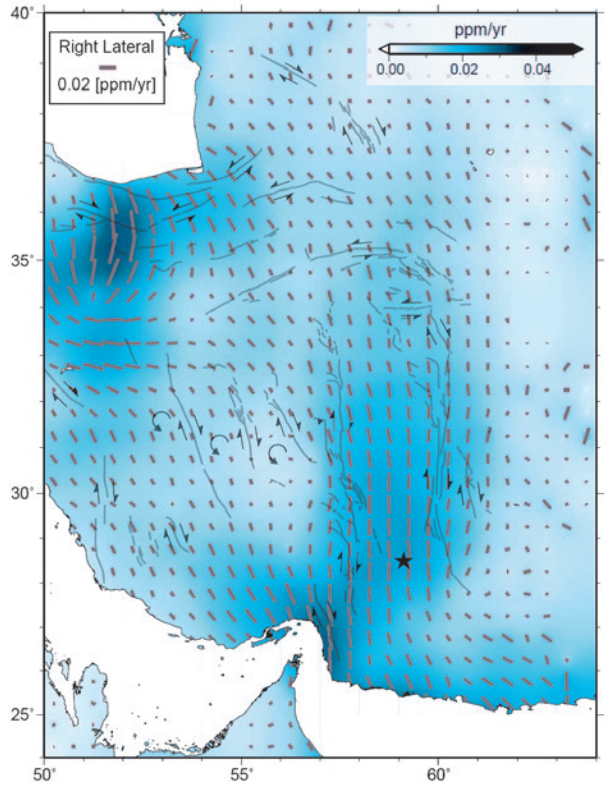

Fig.9 A map showing the distribution of maximum shear strain rate. Lighter color denotes smaller values. Solid lines represent the direction and magnitude of the right-lateral component. A star indicates the epicenter of the mainshock.

development of the existing active faults. On the other hand, the fault of our studied event is not consistent with the regional strain rate field. Different strain pattern probably distributed in the region locally, however, the GPS sites are too sparsely deployed to estimate the local strain field in and around the source area (Fig. 1).

The NS-oriented faults along the eastern and western borders of the Lut Block are branched approximately 30°N (Fig. 10). The two branches are termed as Kahurak fault and Bam fault, respectively. Although no active fault is known in and around the source region, the fault of the mainshock is on the southern extension of the Kahurak fault (Fig. 10). Considering the inferred strike and fault motion type (right-lateral), the causative fault of this event is probably the identical fault system to the Kahurak fault. There are no geologically mapped major faults in the source region, however, our studied inland earthquakes indicate that the collision of the Arabian and Eurasian plates.

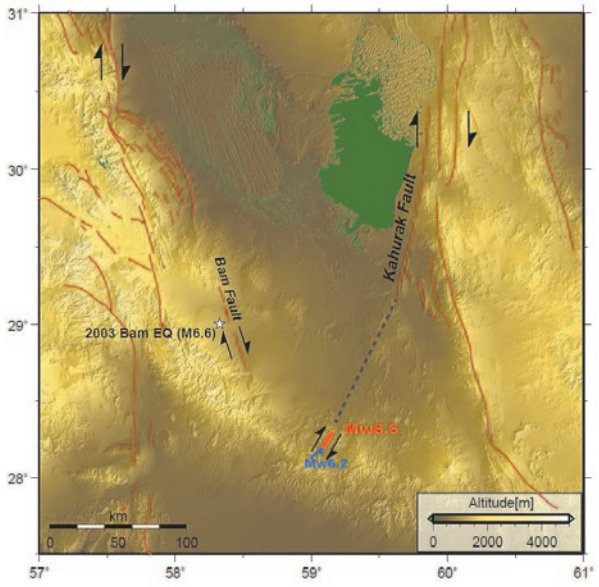

Fig.10 Spatial relationship between the inferred fault of the M6.6 and M6.2 events and the surrounding active faults.

7. Concluding remarks

We applied InSAR analysis using ALOS/PALSAR data for the 2010 southeastern Iran earthquake (M6.5). The following conclusions are obtained from the analysis:

1. An intensive deformation is located approximately 100 km southeast from the epicenter of the 2003 Bam earthquake.

2. Clear crustal deformation is detected from both the ascending and descending orbits, with a slant range change of ~25 cm at maximum.

3. According to the 2.5D displacement field analysis, the fault motion is right-lateral slip with the NE-SW-oriented strike.

4. A fault model which consists of a rectangular fault with a uniform slip in an elastic half-space shows (1) a nearly vertical fault plane, (2) a NE-SW strike direction, (3) a nearly pure right-lateral fault motion, and (4) a moment magnitude of 6.6.

5. The fault of the mainshock is on the southern extension of the Kahurak fault, suggesting that the causative fault of this event is probably the identical fault system to the Kahurak fault.

Acknowledgments

PALSAR data are provided from Earthquake

Working Group under a cooperative research contract with JAXA (Japan Aerospace Exploration Agency). The ownership of PALSAR data belongs to JAXA and METI (Ministry of Economy, Trade and Industry). We used GMT (Generic Mapping Tools) provided by Wessel and Smith (1991) for figure construction.

References

Berberian, M. and Yeats, S.R. (1999): Patterns of Historical Earthquake Rupture in the Iranian Plateau. Bulletin of Seismological Society of America, 89, 1, 120-139.

Bürgmann, R., P. A. Rosen and E. J. Fielding (2000): Synthetic Aperture radar interferometry to measure Earth's surface topography and its deformation, Annu. Rev. Earth Planet. Sci., 28, 169– 209.

Cervelli, P., M. H. Murray, P. Segall, Y. Aoki and T. Kato (2001): Estimating source parameters from deformation data, with an application to the March 1997 earthquake swarm off the Izu Peninsula, Japan, J. Geophys. Res., 106, 11217-11237.

Efron, B. (1979): Bootstrap methods: another look at the jacknife, Annals of Statistics, 7, 1-26.

Freund, R. (1970): Rotation of strike-slip faults in Sistan, southeast Iran. Journal of Geology 78, 188–200.

Fujiwara, S., T. Nishimura, M. Murakami, H. Nakagawa, M. Tobita and P. A. Rosen (2000): 2.5-D surface deformation of M6.1 earthquake near Mt Iwate detected by SAR interferometry, Geophys. Res. Lett., 27, 2049-2052.

Fujiwara S. and M. Tobita (1999): SAR interferometry techniques for precise surface change detection, J. Geod. Soc. Japan, 45, 283-295 (in Japanese with English abstract).

Fujiwara, S., M. Tobita, M. Murakami, H. Nakagawa and P. A. Rosen (1999): Baseline determination and correction of atmospheric delay induced by topography of SAR interferometry for precise surface change detection, J. Geod. Soc. Japan, 45, 315-324 (in Japanese with English abstract).

Jónsson, S., H. Zebker. P. Segall and F. Amelung (2002): Fault slip distribution of the 1999 M7.2 Hector Mine earthquake, California, estimated from satellite radar and GPS measurements, Bull. Seism. Soc. Amer., 92, 1377-1389.

Kobayashi, T. (2009): Experiment in estimate of strain field using a kriging method, Geophys. Bull. Hokkaido Univ., 72, 257-268 (in Japanese with English abstract).

Massonnet, D. and K. L. Feigl. (1995): Discrimination of geophysical phenomena in satellite radar interferograms, Geophys. Res. Lett., 22, 1537-1540.

Massonnet, D. and K. L. Feigl (1998): Radar interferometry and its application to changes in the earth's surface, Rev. Geophys., 36, 441– 500.

Meyer B. and Dortz K. L. (2007): Strike-slip kinematics in Central and Eastern Iran: Estimating fault slip-rates averaged over the Holocene, Tectonics, 26, doi:10.1029/2006TC002073.

Mohajer-Ashjai A, H. Behzadi and M. Berberian (1975): Reflections on the rigidity of the Lut Block and recent crustal deformation in Eastern Iran, Tectonophysics, 25, 281–301.

Okada, Y. (1992): Internal deformation due to shear and tensile faults in a half space, Bull. seism. Soc. Am., 82, 1018–1040.

Rosen, P. A., S. Hensley, F. Li, I. Joughin, S. Madsen and D. Goldstein (2000): Synthetic Aperture Radar Interferometry, Proc. IEEE, 88, 333-382.

Tirrul, R., R. Bell, R. J. Griffis and V. E. Camp (1983): The Sistan suture zone of eastern Iran. Geological Society of America Bulletin, 94, 134-150.

Tobita M., S. Fujiwara, M. Murakami, H. Nakagawa and P. A. Rosen (1999): Accurate offset estimation between two SLC images for SAR interferometry, J. Geod. Soc. Japan, 45, 297-314 (in Japanese with English abstract).

Tobita, M. (2003): Development of SAR interferometry analysis and its application to crustal deformation study, J. Geod. Soc. Japan, 49, 1-23 (in Japanese with English abstract).

Tobita, M., T. Nishimura, T. Kobayashi, K. X. Hao and Y. Shindo (2011): Estimation of coseismic deformation and a fault model of the 2010 Yushu earthquake using PALSAR interferometry data, Earth Planet. Sci. Lett., doi:10.1016/j.epsl.2011.05.017.

U. S. Geological Survey (2010): 2010. Magnitude

6.5 - SOUTHEASTERN IRAN 2010 December 20 18:41:59 UTC, http://earthquake.usgs.gov/earthquakes/eqinthenews/2010/usc0000rak (accessed 24 Nov.2011).

Vernant Ph., F. Nilforoushan, D. Hatzfeld, M.R. Abbassi, C. Vigny, F. Masson, H. Nankali, J. Martinod, M. Ghafory-Ashtiany, R. Bayer, F. Tavakoli and J. Chéry (2004): Present-Day Crustal Deformation and Plate Kinematics in the Middle East Constrained by GPS Measurements in Iran and Northern Oman, Geophys. J., Int., 157, 381-398.

Walker R. and Jackson J. (2002): Offset and evolution of the Gowk fault S.E. Iran: a major intracontinental strikeslip system. Journal of Structural Geology 24, 1677-1698.

Walker R. and Jackson J. (2004): Active tectonics and late Cenozoic strain distribution in central and eastern Iran, Tectonics, 23, doi:10.1029/2006TC001529.

Wessel, P. and W. H. Smith (1991): Free software helps map and display data, EOS Trans., AGU, 72(41), 441, 445-446.